



Impedance analysis of porous carbon electrodes to predict rate capability of electric double-layer capacitors

Hyun Deog Yoo ^a, Jong Hyun Jang ^{b,*}, Ji Heon Ryu ^c, Yuwon Park ^a, Seung M. Oh ^{a,*}

^a Department of Chemical and Biological Engineering, Seoul National University, 599 Gwanangno, Gwanak-gu, Seoul 151-744, Republic of Korea

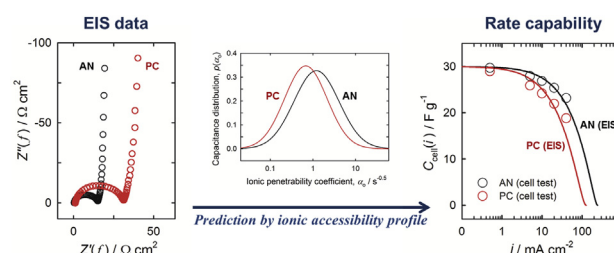
^b Fuel Cell Research Center, Korea Institute of Science and Technology (KIST), Seoul 136-791, Republic of Korea

^c Graduate School of Knowledge-based Technology and Energy, Korea Polytechnic University, 2121 Jeongwang-dong, Siheung-si, Gyeonggi-do 429-793, Republic of Korea

HIGHLIGHTS

- Rate capability of EDLC was quantitatively predicted by an impedance measurement.
- Ohmic resistance and pores' ionic accessibility were factorized by EIS.
- From the two factors, ohmic voltage drop and utilizable capacitance was derived.
- A key formula was devised to correlate the ac with dc information of EDLC.
- Thus predicted rate capabilities were verified by comparing with cell test results.

GRAPHICAL ABSTRACT



ARTICLE INFO

Article history:

Received 29 November 2013

Received in revised form

7 May 2014

Accepted 8 May 2014

Available online 3 June 2014

Keywords:

Electric double-layer capacitor (EDLC)
Electrochemical impedance spectroscopy (EIS)
Rate capability
Porous electrode
Transmission-line model with pore size distribution (TLM-PSD)
Activated carbon

ABSTRACT

Electrochemical impedance analysis is performed to predict the rate capability of two commercial activated carbon electrodes (RP20 and MSP20) for electric double-layer capacitor. To this end, ac impedance data are fitted with an equivalent circuit that comprises ohmic resistance and impedance of intra-particle pores. To characterize the latter, ionic accessibility into intra-particle pores is profiled by using the fitted impedance parameters, and the profiles are transformed into utilizable capacitance plots as a function of charge–discharge rate. The rate capability that is predicted from the impedance analysis is well-matched with that observed from a charge–discharge rate test. It is found that rate capability is determined by ionic accessibility as well as ohmic voltage drop. A lower value in ionic accessibility for MSP20 is attributed to smaller pore diameter, longer length, and higher degree of complexity in pore structure.

© 2014 Elsevier B.V. All rights reserved.

1. Introduction

Electric double-layer capacitors (EDLCs) have been used as a high-power energy storage device due to their unique characteristics of high rate capability (<1 min charge–discharge) and long

* Corresponding authors. Tel.: +82 2 880 7074; fax: +82 2 872 5755.

E-mail addresses: jhjang@kist.re.kr (J.H. Jang), seungoh@snu.ac.kr (S.M. Oh).

cycle life (>100,000 cycles). At present, activated carbons are the most popular EDLC electrodes due to their high electrical conductivity, large surface area and wide pore size distribution [1].

In general, the rate capability of activated carbon electrodes is governed by two factors: 1) ohmic resistance that determines the ohmic voltage drop and thus working voltage, and 2) ionic accessibility into pores, by which utilizable capacitance is determined. Commonly, dc methods are employed to assess the rate capability; for instance, galvanostatic charge–discharge cycling with varied current density. Here, the ohmic resistance (R_{ohm}) can be estimated from the voltage drop at the beginning of current reversal, whereas the ion accessibility can be estimated from the delivered capacitance values. Even if the dc methods can give general information on EDLC parameters, ac methods such as electrochemical impedance spectroscopy (EIS) can provide more detailed information; for instance, pore structure of electrode materials and kinetics in double-layer charging/discharging processes [2]. In the previous works, ac impedance analysis based on transmission-line model with pore size distribution (TLM-PSD) was successfully utilized to assess the pore structure of carbon materials [3–5]. Later on, the concept of TLM-PSD has been incorporated into complex capacitance analysis, which allows a graphical analysis on capacitance, rate capability, and leakage current [6–15]. Especially, it was demonstrated that the effect of pore structure, electrode potential, and electrode thickness on rate capability can be easily evaluated by comparing the peak frequency on imaginary capacitance plots.

The primary objective of this work is to establish an analytical method to correlate the ac method (impedance analysis) with dc method (galvanostatic charge–discharge cycling) for the prediction of rate capability of EDLC systems. To this end, experimental ac impedance data are analysed to obtain ohmic resistance and ionic accessibility for activated carbon electrodes. Then, the utilizable capacitance is calculated as a function of operating time (t_{op}) or current density (i) by using correlation functions between ac and dc variables. Finally, the transform technique is validated by comparing the rate capability predicted from two methods.

2. Experimental details

2.1. Material characterizations

The samples were characterized by using a field-emission scanning electron microscope (FE-SEM, JEOL JSM-6700F), nitrogen adsorption (Micromeritics, ASAP 2010), and small angle X-ray scattering (SAXS, Bruker GADDS, $\text{CuK}\alpha$, $\lambda = 0.154056$ nm). The nitrogen adsorption data was analysed by Barret–Joyner–Halenda (BJH) and modified micropore (MP) [16,17] methods to characterize mesopores and micropores, respectively.

2.2. Electrode preparation

For the electrochemical tests, the composite electrodes were prepared by coating the slurry of active material (RP20 or MSP20), polytetrafluoroethylene and carboxyl methyl cellulose (PTFE + CMC, 6:4 in mass ratio) binder, and conductive carbon (Super-P) (8:1:1 in mass ratio in deionized water) on a piece of Al foil (thickness = 21 μm). The electrode plates were dried in vacuum oven at 120 °C for 12 h without pressing process. The resultant thickness of the coated film was approximately 40 ± 2 μm with the active mass loading of 1.5 ± 0.1 mg on the electrode area of 0.95 cm^2 .

2.3. Electrochemical measurements and impedance fitting

For a 3-electrode cell test, a home-made cell comprising polyether–ether–ketone (PEEK) body and stainless steel (316L) current

collectors was used. A spring was attached to a current collector to keep the positive, negative, and reference electrodes be tightly contacted to the current collectors. O-rings (Viton®) were used to ensure the sealing at the joints of current collectors and cell body. Positive and negative electrodes were positioned to exactly confront each other, and the reference electrode was just beside them. Two pieces of separator was put between positive, reference, and negative electrodes for all the electrodes to be insulated one another. Activated carbon (RP20) were utilized to prepare a reference electrode [18] (coated film on Al foil, 1 mg on 0.6 cm^2 , 50 μm thickness) and a counter electrode (sheet-type, 30 mg on 1.8 cm^2 , 400 μm thickness). A porous glass fibre was used as the separator. The electrolytes were 1 M tetraethylammonium tetrafluoroborate (TEABF_4) in acetonitrile (AN) or propylene carbonate (PC). Impedance was measured at 0.0 V vs. carbon over the frequency range of 2 mHz–100 kHz (Zahner, Im6e) with a root mean square (rms) amplitude of 5 mV. For the complex nonlinear least squares (CNLS) fitting of the impedance data, the TLM-PSD was coded in FORTRAN to run in LEVM 8.09 software [19]. Modulus weighting (with respect to calculated values) was adopted for the CNLS fitting.

For rate experiment, symmetric 2-electrode (CR2032 coin type) cells were assembled by sandwiching two identical electrodes and operated in 0–3.5 V. Experimental conditions are same with the 3-electrode experiments, except for the electrode area (2.27 cm^2). Galvanostatic charge–discharge cycling was made with a WBCS-3000 battery cyler (Wonatech Co.). Both of charging and discharging current densities were varied from 0.5 to 40 mA cm^{-2} .

3. Results and discussion

3.1. Characterization of activated carbons

As the EDLC electrodes, two different activated carbons were used; RP20 (Kuraray Chemical Co.) and MSP20 (Kansai Coke and Chemicals Co.). The former is produced by physical steam activation, whereas the latter by chemical activation using potassium hydroxide (KOH). As shown in the FE-SEM images (inset of Fig. 1a), RP20 has a rougher morphology as compared with that for MSP20. It is known that steam activation (RP20) leads to more severe morphological change as compared with KOH activation (MSP20) [20]. The particle diameter is similar for two carbons (~5 μm).

From the nitrogen adsorption isotherms, total pore volumes (V_{total}) are calculated to be 0.77 $\text{cm}^3 \text{g}^{-1}$ (RP20) and 0.98 $\text{cm}^3 \text{g}^{-1}$ (MSP20) (Table 1). The adsorption–desorption isotherms (Fig. 1a) also show that RP20 has a larger portion of mesopores and macropores, while the micropores are dominant in MSP20. The BET surface area (S_{BET}) is larger for MSP20 due to the higher population of micropores. In the BJH pore size distribution (Fig. 1b), RP20 shows a larger portion of meso- or macropore volume between the diameters of 4–300 nm. The meso- and macro-pore volume at $D > 2$ nm are 0.17 $\text{cm}^3 \text{g}^{-1}$ for RP20 and 0.15 $\text{cm}^3 \text{g}^{-1}$ for MSP20, which is 22% and 15% of V_{total} , respectively. Accordingly, the average mesopore diameter (D_{meso}) is calculated to be larger for RP20 (4.9 nm) as compared with that for MSP20 (2.8 nm). When the micropore region ($D < 2$ nm) is analysed by the modified MP method (Fig. 1c), larger portion of micropore volume is calculated for MSP20 (0.83 $\text{cm}^3 \text{g}^{-1}$, 85%) compared to RP20 (0.60 $\text{cm}^3 \text{g}^{-1}$, 78%).

Pore complexity is compared for two activated carbons by using SAXS technique (Fig. 1d). In the Porod region, the slope in logarithmic scale (Porod slope, z) is related with the fractal dimension (d) of pores by: Intensity (q) $\sim q^{-(6-d)} = q^{-z}$. The theoretical Porod slope is 4 for an ideal flat surface, but the slope gradually decreases to approach 1 with an increase in pore complexity [21]. From the Porod slopes in this work (ca. 2.2 for RP20 and 1.4 for MSP20), it can be assumed that MSP20 has a more complex pore structure.

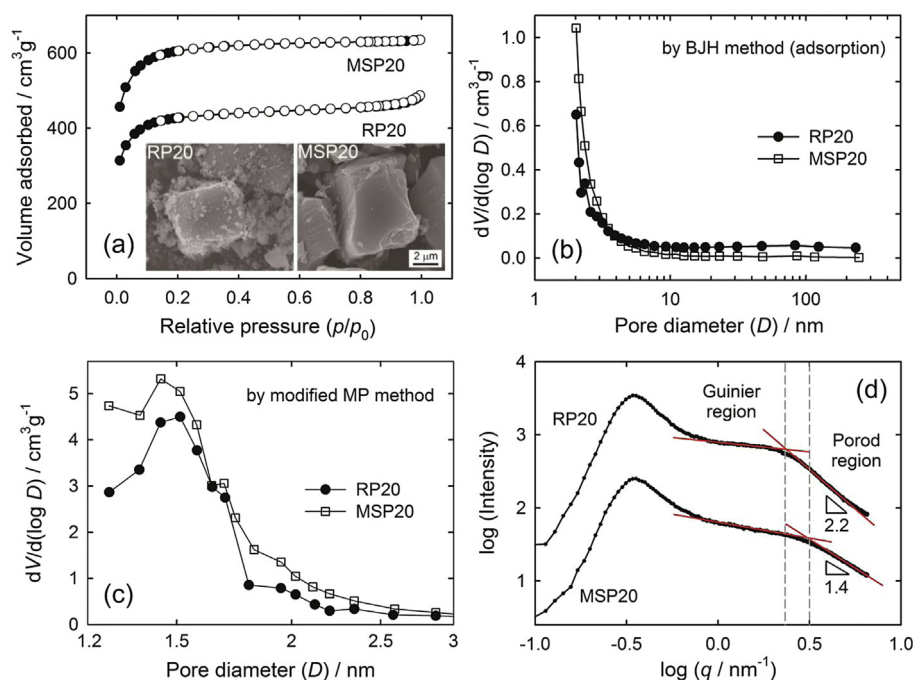


Fig. 1. (a) N₂ adsorption isotherms and pore size distribution by (b) BJH and (c) modified MP methods for RP20 and MSP20. (d) SAXS patterns of RP20 and MSP20. FE-SEM images of RP20 and MSP20 in the inset.

Based on the above results, it is expected that RP20 exhibits higher rate capability since it has larger pore size and lower pore complexity [22], but lower specific capacitance as its surface area is smaller than that for MSP20. Meanwhile, if the specific capacitance is calculated with an assumption that the whole surface is utilized for charge storage with identical capacitance of $8 \mu\text{F cm}^{-2}$ [23,24], it is estimated to be 120 F g^{-1} (RP20) and 160 F g^{-1} (MSP20) from the BET surface areas. However, the calculated value is only a rough estimation since the pore utilization and unit capacitance are strongly dependent on the used electrolyte and charge/discharge rate in practical EDLCs.

3.2. Graphical analysis of EIS data: Nyquist plot and complex capacitance analysis

Fig. 2 displays the Nyquist plots that are obtained from RP20 and MSP20 in 1.0 M TEABF₄/AN and TEABF₄/PC electrolyte, in which a semicircle and a spike appear at the high and low frequency region, respectively. Total impedance can be divided into three components in the Nyquist plots; bulk electrolyte resistance (x -intercept at the highest frequency region), interfacial impedance between electrode and bulk solution (semicircle at the middle frequency region), and the impedance that is associated with intra-particle pores (spike at the low frequency region) (Fig. 3). The first two terms are mainly dependent on the electrolyte solution, while the last one (low frequency tails) is controlled by both electrode materials and electrolytes.

Table 1

Pore properties derived from nitrogen adsorption isotherms.

	$S_{\text{BET}}/\text{m}^2 \text{ g}^{-1a}$	$V_{\text{total}}/\text{cm}^3 \text{ g}^{-1}$	D_{avg}/nm	$D_{\text{meso}}/\text{nm}^b$
RP20	1520 ± 30	0.77	2.0	4.9
MSP20	2060 ± 40	0.98	1.9	2.8

^a Measured by Brunaur–Emmett–Teller (BET) method.

^b Measured by Barret–Joyner–Halenda (BJH) method.

Previously, the semicircle at the middle frequency region has been assigned to the ion transport processes [25–27] or the contact impedance between electrode and current collector [28,29]. As the resistances are larger in the PC-based electrolyte for both electrodes in this work, the ion transport processes seem to be dominant in our experiment, even if the contribution from the electronic contact resistance cannot be neglected. The semicircle has also been assigned to the inter-particle ionic impedance [25], but our simulation shows that the inter-particle ionic resistances are merged in the sloped line at low frequencies as additional pore resistances [9]. Practically, the process for the semi-circle can be regarded as a simple resistance at lower frequency than 10 Hz, while the typical EDLC charge/discharge condition corresponds to the frequency of 0.1 Hz.

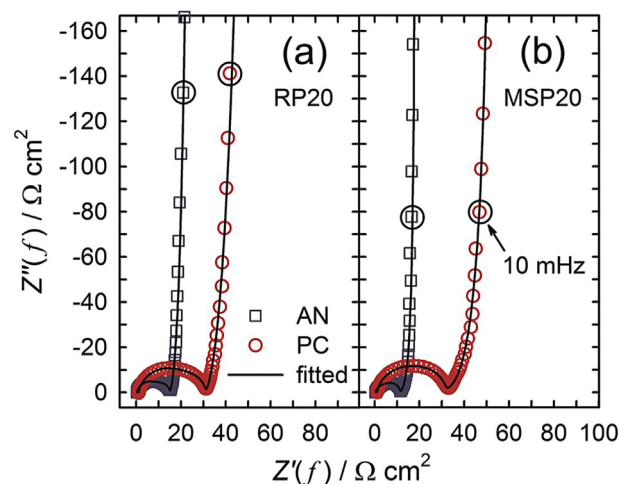


Fig. 2. Nyquist plots of (a) RP20 and (b) MSP20 electrodes in AN or PC electrolytes. Lines: CNLS fitted results.

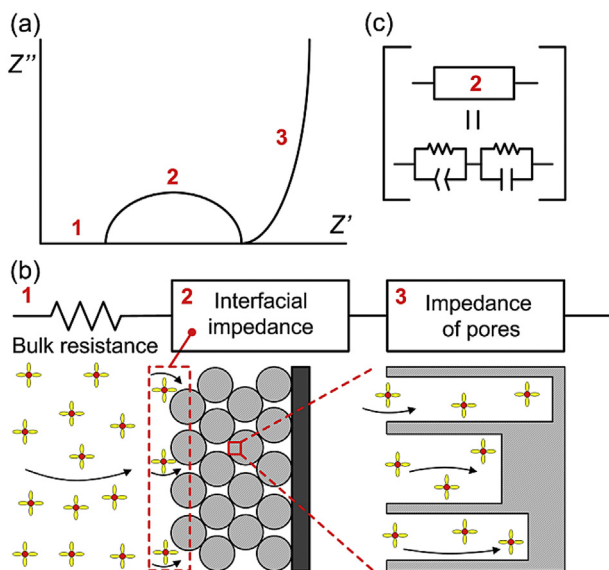


Fig. 3. Equivalent circuit model for the porous carbon electrodes.

As a simple approach, capacitive electrochemical systems can be represented by a serial connection of equivalent series resistance (R_{esr}) and utilizable capacitance (C_{util}), which approximates the capacitor behaviour at sufficiently low frequencies. In this approximation, R_{esr} comprises 1) bulk electrolyte resistance, 2) interfacial resistance, and 3) apparent resistance of intra-particle pores (Fig. 3). The capacitive charge storage is assumed to occur on electrochemically equivalent sites with identical serial resistance. As the impedance of such circuit is $R_{\text{esr}} - j/(\omega C_{\text{util}})$, where j is imaginary unit and ω is angular frequency ($=2\pi f$), the R_{esr} and C_{util} can be determined from the real and imaginary part of experimental impedance data from the perpendicular region in the Nyquist plots (Fig. 2).

In the AN-based electrolyte (ionic conductivity = 56 mS cm^{-1} at 25°C), from the impedance data at 10 mHz, the R_{esr} and C_{util} are calculated to be $21 \Omega \text{ cm}^2$ and 80 F g^{-1} for RP20, and $17 \Omega \text{ cm}^2$ and 140 F g^{-1} for MSP20. In the PC-based electrolyte (ionic conductivity = 13 mS cm^{-1} at 25°C), the R_{esr} and C_{util} are calculated

to be $42 \Omega \text{ cm}^2$ and 75 F g^{-1} for RP20, and $47 \Omega \text{ cm}^2$ and 130 F g^{-1} for MSP20. Here, mass (g) refers to mass of carbon only (i.e. without the mass of aluminium current collector). As higher rate capability can be assumed by smaller time constant (τ) that is the product of R_{esr} and C_{util} , it is predicted that the rate capability of RP20 (τ : 2.6 s in AN and 4.7 s in PC) is higher as compared with that for MSP20 (τ : 3.5 s in AN and 9.1 s in PC). Rate capability can be predicted from this simple graphical analysis by using R_{esr} and C_{util} values, but detailed analysis, such as the separate discussion on the effect of ion size and conductivity, is not available.

More detailed analysis on the capacitive parameters and rate capability can be performed by using the complex capacitance analysis [7]. For this, the measured impedance ($Z(f) = Z'(f) + jZ''(f)$) is transformed into the complex capacitance ($C(f) = C'(f) + jC''(f)$) by the relation of $C(f) = 1/[j\omega Z(f)]$. The real part of complex capacitance ($C'(f)$) represents the apparent capacitance value as a function of frequency, while the imaginary part ($C''(f)$) is correlated with $C'(f)$ by Kronig–Kramers (K–K) relations. When $C''(f)$ is plotted as a function of frequency in semi-log scale, peak-shaped curves are appeared in the imaginary capacitance plot ($C''(f)$ vs. $\log f$, Fig. 4a and b). Then, as suggested by the K–K relations, total capacitance (C_{tot}) can be calculated from the peak area (A_p) as $C_{\text{tot}} = 1.466A_p$ [13]. In addition, the peak frequency (f_p) at the maximum $C''(f)$ corresponds to the characteristic frequency, which is inversely proportional to the time constant (τ) of capacitive systems. Therefore, capacitance and rate capability can be easily estimated from this graphical analysis.

Fig. 4a and b presents the imaginary capacitance plots obtained from two activated carbon electrodes. The C_{tot} and f_p values are determined to be $83.2 \text{ F g}^{-1}/70.7 \text{ mHz}$ (RP20) and $140.4 \text{ F g}^{-1}/50.4 \text{ mHz}$ (MSP20) in the AN-based electrolyte; and $79.2 \text{ F g}^{-1}/34.9 \text{ mHz}$ (RP20), and $143.0 \text{ F g}^{-1}/16.6 \text{ mHz}$ (MSP20) in the PC-based electrolyte (Table 2). The C_{tot} values are comparable in two electrolytes, but they were smaller than the estimations from the BET surface area (i.e. 120 and 160 F g^{-1} for RP20 and MSP20, respectively; assuming $8 \mu\text{F cm}^{-2}$ for carbon surface) for both RP20 (~69%) and MSP20 (~89%) because very small pores that are not utilizable for ion adsorption are also detected by N_2 molecules (BET). This finding supports that EDLC can be more properly evaluated by electrochemical method that utilizes actual ions as the probe molecule, compared to N_2 adsorption method that uses N_2 as the probe molecule [5]. Meanwhile, the peak frequency values

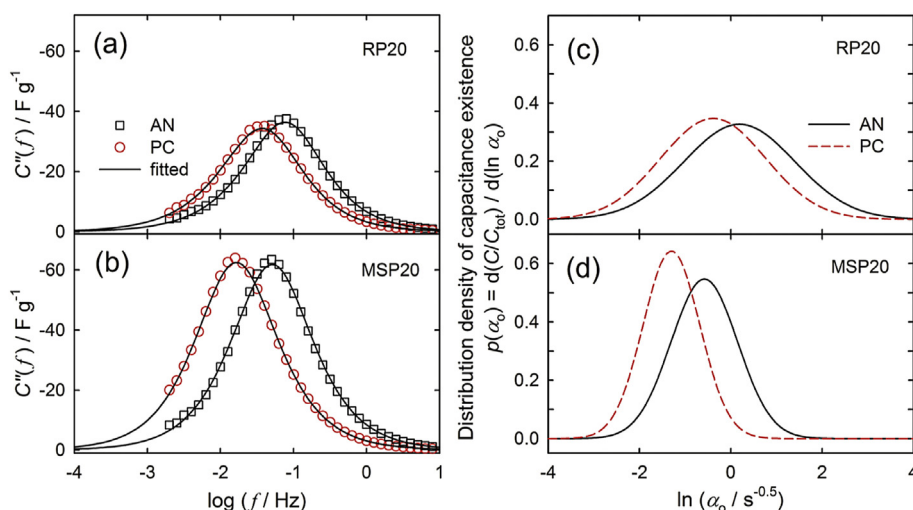


Fig. 4. Imaginary capacitance plots of (a) RP20 and (b) MSP20 electrodes in AN or PC electrolytes with CNLS fitted results. Ionic accessibility profiles for (c) RP20 and (d) MSP20 electrodes with an assumption of log-normal distribution (Eq. (6)).

Table 2

Capacitive parameters derived from imaginary capacitance plots.

		f_p/mHz	$C_{\text{tot}}/\text{F g}^{-1}$	FWHM
RP20	1 M TEABF ₄ /AN	71	83	1.33
	1 M TEABF ₄ /PC	35	79	1.36
MSP20	1 M TEABF ₄ /AN	50	140	1.33
	1 M TEABF ₄ /PC	17	143	1.35

indicate that rate capability of RP20 is higher than that of MSP20 in both electrolytes by a factor of 1.4 (AN) and 2.1 (PC). This solvent-dependent rate capability for two carbon electrodes can be ascribed to the difference in the solvated ionic diameter: *ca.* 1.2 nm for AN and 1.4 nm for PC [30].

3.3. Ionic accessibility profile by CNLS fitting

A schematic Nyquist plot is presented in Fig. 3a. At the high frequency limit, a resistive term appears due to ion transport in bulk solution, which can be represented by a simple resistance of R_{bulk} (Fig. 3b). The semicircle in the middle frequency region is assigned to the ion migration across the bulk-electrolyte/electrode interface, while the sloping spike at the low frequency region is for the combined effect of ion transport and double-layer formation inside pores. As these processes are serially connected, total impedance ($Z(f)$) is the sum of bulk resistance (R_{bulk}), impedance for the semicircle ($Z_{\text{interface}}$) and sloping spike ($Z_{\text{intra-pore}}$):

$$Z(f) = R_{\text{bulk}} + Z_{\text{interface}}(f) + Z_{\text{intra-pore}}(f) \quad (1)$$

To simulate the interfacial impedance ($Z_{\text{interface}}$), (R_1Q_1)(R_2C_2) circuit (Fig. 3c) is used, where Q is the constant phase element (CPE, $Z_{\text{CPE}} = 1/[T(j\omega)^p]$) [31]. The R_2C_2 is added because the depressed semicircles are not successfully fitted by the R_1Q_1 alone. In the fitting, p is *ca.* 0.9 for all the fitted results and T is a variable. For the $Z_{\text{intra-pore}}$, the cylindrical pore model is utilized, in which the equivalent circuit follows the TLM with segmental ionic resistances and surface capacitances in intra-particle pores [32]. For a single pore or uniform multiple pores, the electrochemical characteristics with ac signals ($C_{\text{TLM}}(f, \alpha_0)$) can be expressed as the product of total capacitance (C_{tot}) and the characteristic function ($C^0(f, \alpha_0)$) as:

$$C_{\text{TLM}}(f, \alpha_0) = C_{\text{tot}} \times C^0(f, \alpha_0) \quad (2)$$

$$C^0(f, \alpha_0) = \frac{\alpha_0}{\sqrt{j\pi f}} \tanh\left(\frac{\sqrt{j\pi f}}{\alpha_0}\right) \quad (3)$$

$$\alpha_0 = \frac{1}{2} \sqrt{\frac{\kappa r}{C_d l^2}} \quad (4)$$

Here, the ionic accessibility (α_0) indicates the feasibility for ac signal to penetrate into pores (radius: r , and length: l) when the ionic conductivity in pores is κ and the capacitance per unit area on pore surface is C_d (Eq. (4)). For a pore with an α_0 , the frequency dependency of the capacitance utilization can be represented by Eq. (3).

The uniform pore model fails to analyse practical porous carbon electrodes since pore structures are significantly non-uniform, except for some highly ordered materials [3]. Therefore, it is necessary to consider the non-uniformity of pores in modelling the electrochemical characteristics of porous carbon electrodes. When $p(\alpha_0)$ is the ionic accessibility profile as a function of ionic accessibility, the complex capacitance of non-uniform multiple pores ($C_{\text{TLM-PSD}}(f)$), with total capacitance of C_{tot} , is given as follows [7]:

$$C_{\text{TLM-PSD}}(f) = C_{\text{tot}} \int_{-\infty}^{\infty} C^0(f, \alpha_0) p(\alpha_0) d \ln \alpha_0 \quad (5)$$

Based on Eq. (5), the ionic accessibility profile, $p(\alpha_0)$, can be obtained by de-convoluting the impedance data with discrete Fourier transform [7,33]. However, it has been reported that the PSD of porous materials can be assumed to have log-normal function (Eq. (6)) to reasonably fit the experimental EIS data, where α_0^* and σ represent the characteristic ionic accessibility and the degree of distribution for the electrode, respectively [3–5].

$$p(\alpha_0) = \frac{1}{\sqrt{2\pi}\sigma} \exp\left[-\frac{1}{2\sigma^2}(\ln \alpha_0 - \ln \alpha_0^*)^2\right] \quad (6)$$

The experimental impedance data of RP20 and MSP20 electrodes are CNLS fitted by Eq. (1), assuming non-uniform multiple pores with log-normal distribution (Eq. (6)). The $Z_{\text{intra-pore}}(f)$ is represented as $1/[j\omega C_{\text{TLM-PSD}}(f)]$ (Eq. (5)). The fitted curves are in a good agreement with the experimental data as shown in Nyquist plots (Fig. 2) and imaginary capacitance plots (Fig. 4a and b). From the optimized parameters (Table 3), the electrochemical characteristics for intra-particle pores can be separately analysed from that of the bulk electrolyte and interface (Table 4).

When the fitted parameters are compared with those from the complex capacitance analysis, total capacitance values are similar within 1% of difference. From the larger α_0^* values, higher rate capability is expected for RP20 in both electrolytes, which is in accordance with the expectation from the f_p values in the graphical analysis. Therefore, it can be concluded that the capacitance and rate capability, which are the key parameters to characterize electrochemical characteristics of porous carbon electrodes, can be successfully analysed by graphical analysis with $C''(f)$ vs. $\log f$ plot, as confirmed by fitted parameters.

The ionic accessibility profile, which enables the quantification of rate capability, is derived by the unique interpretation of the impedance data. The ionic accessibility profile is defined as the distribution density of capacitance existence with respect to the natural log of ionic accessibility ($p(\alpha_0)$ vs. $\ln \alpha_0$), which is obtained from Eq. (6) with the fitted parameters α_0^* and σ (Fig. 4c and d). The distribution function, $p(\alpha_0) = d[C/C_{\text{tot}}]/d[\ln \alpha_0]$, can be interpreted as the distribution densities of surface existence ($d[S/S_{\text{tot}}]/d[\ln \alpha_0]$) if constant C_d is assumed over the entire surface. As the ionic accessibility profile of RP20 is shifted to the higher α_0 direction, it can be noticed that RP20 has more accessible pores by ac signals compared with MSP20. In other words, MSP20 has smaller α_0^* , which is in accordance with the nitrogen adsorption (larger portion of micropores) and SAXS analysis (higher complexity of porous structure) results. The smaller pore diameter, more complex pore structure, and possibly longer average pore length of MSP20 result in the smaller α_0^* value. Of two electrolytes, the AN-based one provides larger α_0^* due to higher ionic conductivity as compared with the PC-based one. All the properties are colligated to α_0^* , the characteristic ionic accessibility into pores, according to Eq. (4). The larger values of σ for RP20 reflect that the pore structure is more largely distributed compared with MSP20.

Table 3

TLM-PSD parameters obtained by fitting the impedance data to Eq. 1

		$C_{\text{tot}}/\text{F g}^{-1}$	$\alpha_0^*/\text{s}^{-0.5}$	σ	χ^2
RP20	AN ^a	82.1 ± 0.2	1.21 ± 0.09	1.22 ± 0.07	7.2 × 10 ^{−3}
	PC	79.0 ± 0.1	0.68 ± 0.01	1.15 ± 0.03	9.1 × 10 ^{−3}
MSP20	AN	139.0 ± 0.2	0.56 ± 0.02	0.73 ± 0.03	7.9 × 10 ^{−3}
	PC	141.5 ± 0.2	0.273 ± 0.001	0.622 ± 0.009	4.2 × 10 ^{−3}

^a All the electrolytes contain 1 M TEABF₄.

Table 4

Parameters corresponding to the impedance of bulk electrolyte and interfaces obtained by fitting the impedance data to Eq. 1

		$R_{\text{bulk}}/\Omega \text{ cm}^2$	$R_1/\Omega \text{ cm}^2$ ^b	$R_2/\Omega \text{ cm}^2$	$T_1/10^{-6}$	p_1	$C_2/\mu\text{F cm}^{-2}$
RP20	AN ^a	0.37 ± 0.01	9.7 ± 0.4	4.7 ± 0.3	68 ± 6	0.89 ± 0.01	420 ± 60
	PC	1.04 ± 0.03	20.6 ± 0.6	6.9 ± 0.6	37 ± 2	0.89 ± 0.01	260 ± 30
MSP20	AN	0.43 ± 0.02	4.4 ± 0.5	5.1 ± 0.5	70 ± 10	0.88 ± 0.02	80 ± 20
	PC	1.02 ± 0.02	19.6 ± 0.6	9.5 ± 0.6	46 ± 2	0.88 ± 0.01	140 ± 20

^a All the electrolytes contain 1 M TEABF₄.^b R_n stands for interfacial resistance of n th semicircle, T_1 and p_1 for CPE parameters of 1st semicircle, and C_2 for interfacial capacitance of 2nd semicircle.

3.4. Differential and apparent capacitances calculated from ionic accessibility profiles

From the ionic accessibility profiles (Fig. 4c and d), the rate capability of two activated carbon electrodes can be predicted. To this end, firstly, the utilization of cylindrical pores with an ionic accessibility of α_0 , at an operating ac frequency of f_{op} , is assumed to be $\text{Re}[C^0(f_{\text{op}}, \alpha_0)]$ based on the TLM (Eq. (3)). Then, with a decrease in f_{op} , the utilization of a single pore will gradually increase from 0 (high frequency limit) to 1.0 (low frequency limit). Theoretically, the pore utilization will be 10%, 50%, and 90% at f_{op}/α_0^2 of 15.9, 0.991, and 0.294, respectively (Fig. S1).

As the porous carbon electrodes have non-uniform pores, the differential specific capacitance of an electrode, as a function of f_{op} , can be calculated from the EIS data ($C_{\text{diff,EIS}}(f_{\text{op}})$) according to the following integral equation (Eq. (7)), where the $p(\alpha_0)$ represents the ionic accessibility profile obtained from EIS analysis, and $\overline{C_{\text{tot}}}$ the average total capacitance of an electrode in the operating voltage range.

$$C_{\text{diff,EIS}}(f_{\text{op}}) = \overline{C_{\text{tot}}} \int_{-\infty}^{\infty} \text{Re}[C^0(f_{\text{op}}, \alpha_0)] p(\alpha_0) d\ln \alpha_0 \quad (7)$$

If the capacitance is constant over the potential range, the $\overline{C_{\text{tot}}}$ can be determined from the C_{tot} value measured by single EIS analysis at any potential. The most direct method for studying the potential-dependent quantities (e.g. capacitance) is multiple impedance measurement at every potential, which is not practical because each impedance measurement takes at least 2 h for a particular potential point. Alternatively, either cyclic voltammetry (CV) at a slow scan rate or charge–discharge cycling at a slow rate can be performed to measure $\overline{C_{\text{tot}}}$. In this study, using slowly scanned CV, $\overline{C_{\text{tot}}}$ values are determined to be 120 F g^{−1} for RP20 (in AN and PC) and 160 F g^{−1} and 150 F g^{−1} for MSP20/AN and MSP20/PC, respectively (Fig. 5). As the capacitance value is potential-dependent, the measured C_{tot} are 1.1–1.5 times larger than the C_{tot} value obtained from EIS analysis at 0 V vs. carbon. Usually the capacitance of activated carbon electrodes is minimum at the potential of zero charge (pzc, about 0 V vs. carbon) [34]. The lower specific capacitance of MSP20 in PC compared to AN is due to the shrinkage of the voltammogram at about <−1.5 V vs. carbon, which has been explained by either pore-narrowing by ion-induced strain or saturation of the pores by ions before the electrode potential reaches the lower limit [35,36].

Fig. 6a and b shows the $C_{\text{diff,EIS}}(t_{\text{op}})$ curves as a function of operating time (t_{op}) for RP20 and MSP20 electrodes in AN- and PC-based electrolytes. The operating frequency (f_{op}) is transformed into the operating time (t_{op}) in dc techniques by $t_{\text{op}} = 0.5/f_{\text{op}}$, considering the period of ac signal as the time span for a charge and discharge cycle. The $C_{\text{diff,EIS}}(t_{\text{op}})$ curve predicts the differential capacitance as a function of t_{op} . For example, the differential capacitance of an EDLC cell with RP20/AN is expected to be 120 F g^{−1} at slow charge/discharge (t_{op} : 1000 s) and decreased to 109 F g^{−1} at higher rate (10 s). In the case of MSP20 with PC electrolytes, the decrease in

differential capacitance can be predicted to be more severe: 150 F g^{−1} (t_{op} : 1000 s) to 93 F g^{−1} (10 s). Accordingly, the “rate capability” can be quantitatively determined for various combinations of electrode materials and electrolytes. When the operation time of the EDLC cells are decreased from 1000 s to 10 s, the retained capacitances will be: RP20/AN (90.8%) > MSP20/AN (85.8%) > RP20/PC (82.7%) > MSP20/PC (62.0%). In general, the higher the α_0^* value, the more feasible is the operation at shorter t_{op} . In addition to the effect of α_0^* , the $C_{\text{diff,EIS}}(t_{\text{op}})$ curves change less steeper for RP20 with respect to t_{op} , due to the larger σ values (1.2) than those of MSP20 (0.6–0.7). Also, the smaller value of σ for MSP20 leads to the higher susceptibility to the ionic conductivity for the rate capability, which is evidenced by the larger difference of $C_{\text{diff,EIS}}(t_{\text{op}})$ curves by electrolytes for MSP20 (0.64 decade) compared to that of RP20 (0.50 decade) (Fig. 6a and b).

To validate the developed EIS analysis method in a voltage range as wide as possible, symmetrical EDLC cells were constructed and galvanostatic charge–discharge measurements were carried out between 0 and 3.5 V at various current densities ($i = 0.5$ –40 mA cm^{−2}) (Fig. 7). The EDLC cells were evaluated at an operating voltage of 3.5 V, which was used by some groups for higher energy density [37,38]. Note that the 3.5 V operation was used for proof of concept, and the practical operating voltage of EDLC is between 2.5 and 2.8 V, which can provide better durability.

The differential specific capacitances for an electrode, $C_{\text{diff,disch}}(i)$, were determined from the discharge capacity of a symmetric full cell ($Q_{\text{cell,disch}}(i)$) by using following equation. Here, the $C_{\text{diff,disch}}(i)$ is inversely proportional to the slope in the linear region that appears after the IR -drop. In Eq. (8), $Q_{\text{cell,disch}}(i)$ was multiplied by 4

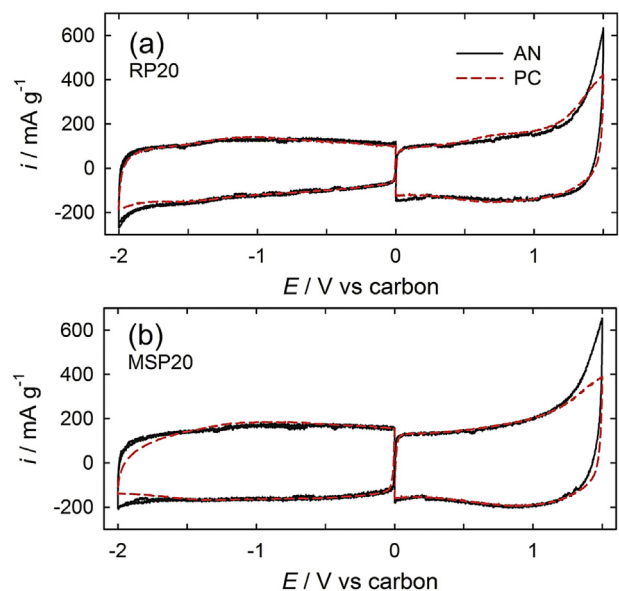


Fig. 5. Cyclic voltammograms of (a) RP20 and (b) MSP20 electrodes in AN and PC electrolytes ($v = 1 \text{ mV s}^{-1}$).

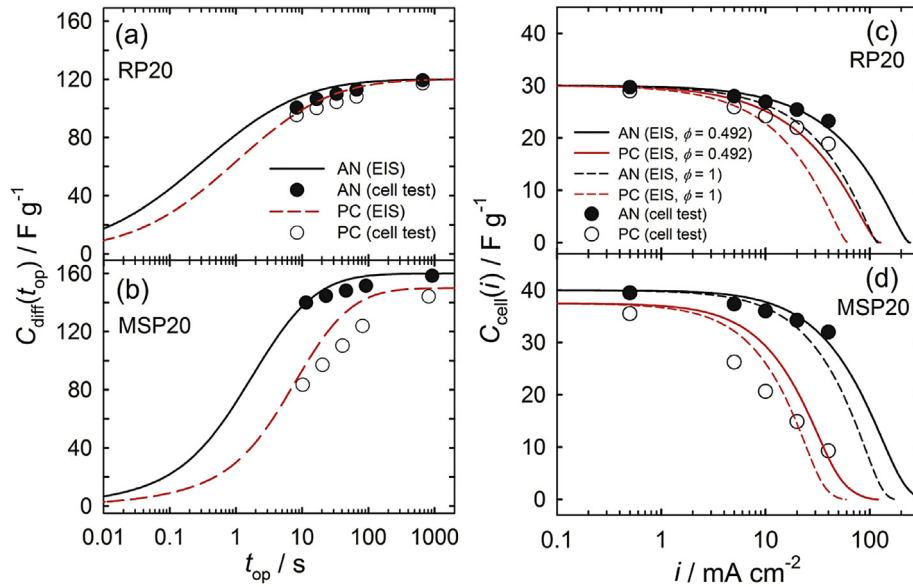


Fig. 6. (a,b) $C_{diff,EIS}(t_{op})$ profiles (lines) with respect to the operational time (t_{op}) and $C_{diff,disch}(t_{op})$ values from the full-cell rate test (points). (c,d) $C_{cell,EIS}(i)$ profiles (dashed lines, $\phi = 1$; solid lines, $\phi = 0.492$) with respect to the current density (i) and the full-cell rate test data ($C_{cell,disch}(i)$, points).

considering that the symmetric EDLC cell contains active mass of both electrodes (i.e. total mass becomes 2 times of an electrode's mass) while the cell's capacitance becomes half of an electrode's capacitance due to the serial connection.

$$C_{diff,disch}(i) = 4 \times Q_{cell,disch}(i) / (V_{op} - V_{ohm}) \quad (8)$$

As shown in Fig. 6a and b, the $C_{diff,disch}(t_{op})$ values, which were measured by the galvanostatic charge–discharge of EDLC cells, were well matched with the $C_{diff,EIS}(t_{op})$ curves predicted by the EIS data in half-cell tests. Here, the operational time is equal to the experimental discharging time. For example, the C_{diff} of an EDLC electrode with RP20/AN was experimentally measured to be $119 F g^{-1}$ ($0.5 mA cm^{-2}$), 110 ($10 mA cm^{-2}$), and 100 ($40 mA cm^{-2}$), which well agrees with the expected values by EIS analysis. For four kinds of EDLCs, the deviation between experimental and predicted values was within 10%. Therefore, it can be concluded that the rate capability of differential capacitance of EDLC cells can be quantitatively predicted by the developed analysis technique of the impedance data for porous electrodes in half cell test.

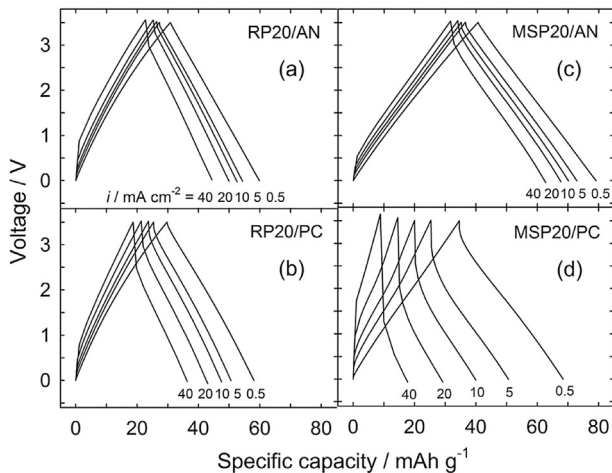


Fig. 7. Charge–discharge curves at various current density (0.5 – $40 mA cm^{-2}$) for (a) RP20 and (b) MSP20 electrodes in AN or PC electrolytes.

In addition to the differential specific capacitance of an electrode (C_{diff}), the apparent specific capacitance of EDLC cells (C_{cell}) and its dependency on the current density are another important factor in evaluating practical EDLC cells. The C_{cell} represents the practical utilizable capacitance of EDLC cells that includes the effect of ohmic losses, whereas the C_{diff} indicates the characteristics of electrode materials. When charge/discharge at various currents (i), the apparent specific capacitance of an EDLC cell ($C_{cell,disch}$) is calculated by dividing the discharging specific capacity of symmetric full-cell, $Q_{cell,disch}(i)$, by the operating voltage (V_{op} , $3.5 V$ in this work) as:

$$C_{cell,disch}(i) = Q_{cell,disch}(i) / V_{op} \quad (9)$$

At slow current density ($5 mA cm^{-2}$), measured $C_{cell,disch}(i)$ values for EDLC cells (points in Fig. 6c and d) are close to one fourth of the $C_{diff,disch}(i)$ values for single electrodes, as expected with negligible iR -drop. With current increase, the $C_{cell,disch}$ values are decreased by increased ohmic drop (V_{ohm}) as well as by the decrease in $C_{diff,disch}$. As a result, the decrease with current is expected to be larger for $C_{cell,disch}$ than $C_{diff,disch}$. For example, when the discharge current was increased from $0.5 mA cm^{-2}$ to $40 mA cm^{-2}$, the $C_{cell,disch}$ was decreased by 74%, while the decrease in $C_{diff,disch}$ was 42%. As the iR -drop plays an important role, the effect of electrolytes on rate capability was much larger for the apparent capacitances ($C_{cell,disch}(i)$). When the electrolyte was changed from AN to PC, the $C_{cell,disch}$ of RP20 was decreased by 19% ($40 mA cm^{-2}$), while the corresponding $C_{diff,disch}$ change was 5%.

The apparent specific capacitance of an EDLC cell, $C_{cell,EIS}$, also can be predicted quantitatively from the $C_{diff,EIS}(t_{op})$ of an electrode determined through the EIS analysis (Eq. (10)). In Eq. (10), $C_{diff,EIS}(t_{op})$ was divided by 4 considering that the symmetric EDLC cell contains 2 times of active mass (i.e. mass of activated carbon) while the capacitance itself becomes half due to the serial connection. For this, the ohmic resistance of EDLCs and operating time should be determined at various current densities.

$$C_{cell,EIS}(i) = Q_{cell,EIS}(i) / V_{op} = \frac{C_{diff,EIS}(t_{op})}{4} \times \frac{V_{op} - iR_{ohm}}{V_{op}} \quad (10)$$

The ohmic resistances of EDLC cells are mainly composed of bulk resistance in organic electrolytes and resistive terms from two electrodes. In the EIS analysis with a three electrode cell, the interfacial impedance ($Z_{\text{interface}}$) of a porous carbon electrode was represented by overlapped semicircles. However, as active frequency of the semicircle (100 kHz–10 Hz) is sufficiently larger than the operational condition (i.e. current density) of EDLCs ($f_{\text{op}} < 0.5$ Hz), the interfacial impedance ($Z_{\text{interface}}$) can be regarded as a simple resistance, $R_{\text{interface}}$. Therefore, the ohmic resistance of an EDLC cell (R_{ohm}) can be calculated from the EIS data as the sum of R_{bulk} and interfacial resistances of both electrodes ($R_{\text{interface}} = 2(R_1 + R_2)$), with an empirical correction factor (ϕ), as:

$$R_{\text{ohm}} = [R_{\text{bulk}} + 2(R_1 + R_2)] \times \phi \quad (11)$$

If the fabrication condition of EDLC cells is identical to that of half-cell test, ϕ will become unity. However, the effective bulk resistances and interfacial resistances can be influenced by the electrode fabrication methods and cell geometry [39]. In such cases, the correction factor ϕ is expected to be determined empirically and can be utilized in the prediction of the EDLC performance from EIS data according to the analysis technique developed in this study.

For each combination of porous carbons and electrolytes, the R_{ohm} value was determined by plotting the ohmic voltage drops in the charge–discharge data as a function of current density (Fig. S2). Then, a linear correlation between R_{ohm} values of symmetrical EDLCs and EIS analysis results ($R_{\text{bulk}} + 2(R_1 + R_2)$) were found among MSP20/AN, RP20/AN, and RP20/PC, and the correction factor ϕ for the used EDLC cells was determined to be 0.492 (Fig. S3). This result implies that the applied pressure was probably higher for the coin-type cell (EDLCs for charge/discharge) compared to the home-made test cell (half-cells for EIS analysis). Even though the applied pressure was not numerically determined, it can be concluded that the effect of cell fabrication method on the ohmic resistance values was maintained similarly in this study and therefore the prediction of R_{ohm} from impedance data is possible with a predetermined correlation factor.

In the case of MSP20/PC, the voltage drop at the charge/discharge reversal and resultantly calculated R_{ohm} was much larger than that expected from the EIS result with $\phi = 0.492$. This seems to be originated from the additional voltage drops at the negative electrode, as experimentally confirmed only for the charge/discharge reversal of MSP20/PC (Fig. 8). Previously, similar phenomenon was reported for nanoporous activated carbon electrode in TEABF₄/PC electrolyte, which was explained by strong adhesion of cations on nanopores [40]. Even though the effect of abnormal adhesion cannot be fully predicted by EIS analysis, such combinations of porous carbon and electrolytes with abnormal ohmic drop will be not suitable for practical applications as EDLC devices with high efficiency.

The operating time (t_{op}) that corresponds to the charge/discharge at various current densities (i) could be determined by utilizing Eq. (12). When t_{op} is large (slow charge/discharge with low i), it will be inversely proportional to the current density (i), where the voltage drop by ohmic drop is negligible and $C_{\text{diff,EIS}}(t_{\text{op}})$ is constantly maintained. In contrast, with fast charge/discharge (high i), t_{op} decline with higher i became more rapid due to both the significant ohmic drop and decrease in $C_{\text{diff,EIS}}(t_{\text{op}})$. The relationship between t_{op} and i are numerically calculated from Eq. (12b) and presented in Fig. S4, where V_{op} is 3.5 V and R_{ohm} is determined by Eq. (11) with $\phi = 0.492$. It is noted that at $i < 10$ mA cm⁻², the t_{op} vs. i profiles of identical activated carbon is very similar, regardless of the used electrolytes.

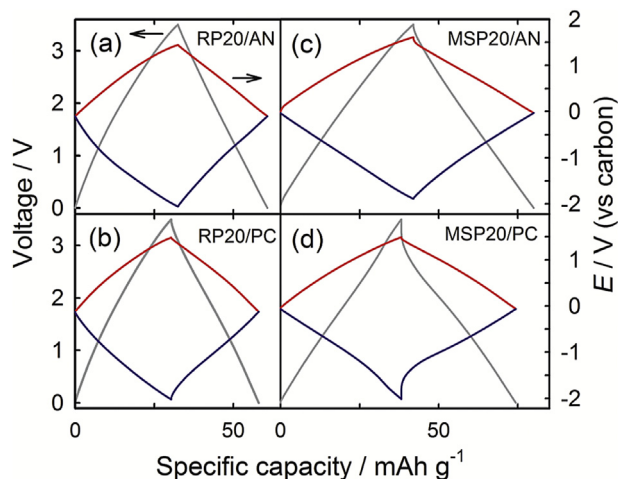


Fig. 8. Potential profiles of both electrodes during the galvanostatic charge–discharge of full cell ($i = 0.5$ mA cm⁻²). Grey: cell voltage. Red and blue: potential of (+) and (–) electrode, respectively. (For interpretation of the references to colour in this figure legend, the reader is referred to the web version of this article.)

$$Q_{\text{cell,EIS}}(i) = \frac{C_{\text{diff,EIS}}(t_{\text{op}})}{4} \times (V_{\text{op}} - iR_{\text{ohm}}) = i \times t_{\text{op}} \times \frac{A}{m} \quad (12a)$$

$$i = \frac{V_{\text{op}}}{R_{\text{ohm}} + 4t_{\text{op}}m^{-1}A / C_{\text{diff,EIS}}(t_{\text{op}})} \quad (12b)$$

Here, A is the apparent electrode area (e.g. 2.27 cm² in this rate experiment) and m is the total active mass in a symmetric EDLC.

Fig. 6c and d compared the apparent specific capacitances calculated from EIS data in comparison to the experimental values. Solid lines in Fig. 6c and d represent thus calculated $C_{\text{cell,EIS}}(i)$ profiles after calibrating the R_{ohm} values with the coefficient of $\phi = 0.492$. The $C_{\text{cell,EIS}}(i)$ and $C_{\text{cell,disch}}(i)$ are matched within 6% deviation for RP20/AN, RP20/PC, and MSP20/AN. When the effect of cell fabrication and geometry was not considered (dashed lines, $\phi = 1$) the calculated values became more deviated from the experimental values, which confirms that the appropriate correction factor is required to utilize EIS data for EDLC cells. The MSP20/PC cell shows larger deviation (up to 33%) even if the R_{ohm} value was calibrated with $\phi = 0.492$, which can be accounted for by limitation in estimating the voltage drop, as described above.

Additionally, charge–discharge curves can be directly simulated from the $C_{\text{diff,EIS}}(i)$ profiles and calibrated R_{ohm} values at a current density (Fig. 9), which are in agreement with experimentally obtained curves except for MSP20/PC. Note that the simulated curves were solely obtained by EIS parameters and C_{tot} parameter from cyclic voltammetry. The simulated and experimental voltage profiles are matched within 3% deviation for RP20 cells, and 4% deviation for MSP20/AN cell. Due to the abnormal adhesion of PC-solvated TEA⁺ ion in MSP20, much larger deviation (41%) was observed for the MSP20/PC cell.

3.5. Applications of EIS analysis of EDLCs for the rate capability prediction and design of capacitor cells

The rate capability from $C_{\text{diff,EIS}}(t_{\text{op}})$ is expected to be the intrinsic properties of activated carbon particles as the extrinsic properties are separated by fitting analysis. In other words, this information is independent of the extrinsic parameters of electrodes (i.e. due to the electrode preparation process), as they are derived solely from the intrinsic parameters of intra-particle pores;

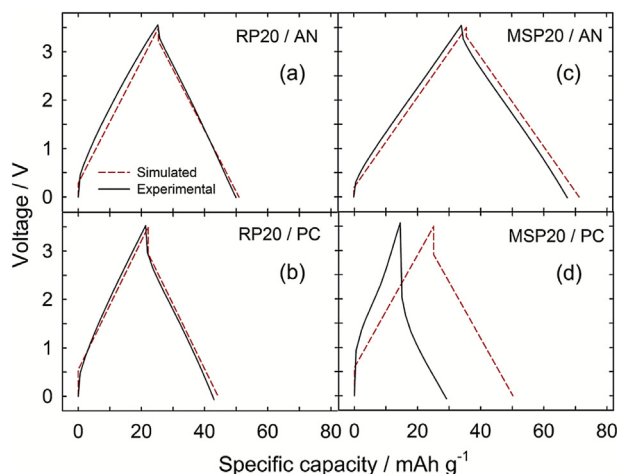


Fig. 9. Comparison of experimental and simulated ($\phi = 0.492$) galvanostatic voltage profiles at $i = 20 \text{ mA cm}^{-2}$.

the precedent impedances that are subject to the experimental conditions are factored out by fitting analysis. And it will be possible to distinguish intrinsic and extrinsic effects on the net rate capabilities of cells that are fabricated by different methods.

The $C_{\text{diff,EIS}}(t_{\text{op}})$ or $C_{\text{cell,EIS}}(t_{\text{op}})$ plots can be applied to estimate the rate capability of a specific cell or to design cells according to the desired specification (*i.e.* operational rate and capacitance). If an EDLC cell is made of MSP20 (10 mg)|1 M TEABF₄ in AN | RP20 (15 mg), the capacitance of positive ($C_{+}(t_{\text{op}})$) and negative ($C_{-}(t_{\text{op}})$) electrodes can be calculated by multiplying active mass to the $C_{\text{diff,EIS}}(t_{\text{op}})$ profiles in Fig. 6a and b. And the capacitance of the full-cell ($C_{\text{fc}}(t_{\text{op}})$) can be calculated according to the rate conditions, by using $1/C_{\text{fc}}(t_{\text{op}}) = 1/C_{+}(t_{\text{op}}) + 1/C_{-}(t_{\text{op}})$.

On the other hand, the $C_{\text{diff,EIS}}(t_{\text{op}})$ curve can be utilized to design a cell with desired rate capability. When 1 Ah of capacity is required at 40 mA cm^{-2} for a 3 V operating symmetric full-cell with $R_{\text{ohm}} = 15 \Omega \text{ cm}^2$, total active mass of porous carbons can be estimated to be 55 g (RP20) or 41 g (MSP20) to fabricate the cell with AN electrolyte from Eq. (8). If R_{ohm} is reduced to $2 \Omega \text{ cm}^2$, the required mass becomes 45 g (RP20) or 33 g (MSP20). This calculation is also possible for the PC-based electrolyte at various discharge rates utilizing the $C_{\text{diff,EIS}}(t_{\text{op}})$ plots. It is noteworthy that, while we try to balance the active mass, the rate capability can be also lowered with thickness increase by several tens of μm [9], where the calculated active mass by the impedance analysis should be regarded as the minimum mass of active materials under no thickness effect. Related future work is to develop more sophisticated model that considers thickness effect.

As this paper aims to represent fundamental ideas for estimation of rate capability, the experiments are simplified. Even if the principles will be the same as described in this paper, there are some specific details to consider before practical application. (1) The rate capability depends on electrode thickness as well as electrode material [9,41–44], but the former effect is not considered in this study. As the effect of electrode thickness can be analysed by similar impedance analysis [9], more precise cell design will be possible through this approach.

(2) Also it is noteworthy that the ionic accessibility profiles are obtained from the impedance measurements at pzc, and the possible differences between the positive and negative electrodes are not represented. If positive and negative electrodes are to be studied separately, impedance should be measured at the middle of the operational potential range for positive and negative electrodes, respectively. This approach can be a future extension of this work.

4. Conclusions

Through the impedance analysis, rate capabilities of porous carbon electrodes are quantitatively profiled as ionic accessibility profile, which is described as the distribution of capacitance with respect to ionic accessibility (α_0). The ionic accessibility profiles are transformed into calculated specific capacitance of an electrode ($C_{\text{diff,EIS}}(t_{\text{op}})$) with respect to operational time (t_{op}). More practically, calculated apparent specific capacitance of a cell ($C_{\text{cell,EIS}}(i)$) was derived from the calculated specific capacitance of an electrode ($C_{\text{diff,EIS}}(t_{\text{op}})$) and calibrated R_{ohm} . The calculated specific capacitance of an electrode ($C_{\text{diff,EIS}}(t_{\text{op}})$) and of a cell ($C_{\text{cell,EIS}}(i)$) are in a good agreement with the galvanostatic full-cell rate test results. This confirms that the rate capabilities of porous carbons can be quantitatively predicted by EIS analysis, considering both intrinsic (*e.g.* $C_{\text{diff,EIS}}(t_{\text{op}})$) and extrinsic (*e.g.* R_{ohm}) factors. The calculated specific capacitance ($C_{\text{diff,EIS}}(t_{\text{op}})$) profile can be used for assessing and designing EDLC cells.

The intrinsic and extrinsic factors that control the EDLC characteristics are separated by their characteristic frequencies or phase-shifts, and obtained quantitatively by fitting the impedance data to appropriate equivalent circuits. This separation-ability of the impedance analysis may lead to the standardized evaluation of porous carbons for EDLC electrodes.

The ionic accessibilities of porous carbons are represented by characteristic ionic accessibility (α_0^*) and the degree of distribution (σ). The pore diameter, existence of subnano-pores or large mesopores, fractal dimension, and average pore length are the factors that control the α_0^* . The smaller the σ value, the higher is the susceptibility to the electrolyte properties (*e.g.* ionic conductivity) for the rate capability. For an electrode with small σ (*e.g.* MSP20 electrode), proper choice of electrolyte is indispensable for the rate capability.

Acknowledgement

This work was supported by the National Research Foundation of Korea funded by the MEST (NRF-2010-C1AAA001-2010-0029065) and the cooperative R&D program funded by the Korea Research Council Industrial Science and Technology (B551179-10-01-00). This work was also supported by the Korea CCS R&D Center (KCRC) grant funded by the Korea Government (Ministry of Science, ICT & Future Planning) (No. 2013038315).

Appendix A. Supplementary data

Supplementary data related to this article can be found at <http://dx.doi.org/10.1016/j.jpowsour.2014.05.058>.

References

- [1] T.A. Centeno, M. Hahn, J.A. Fernandez, R. Kotz, F. Stoeckli, *Electrochem. Commun.* 9 (2007) 1242–1246.
- [2] J. Eskusson, A. Jänes, A. Kikas, L. Matisen, E. Lust, *J. Power Sources* 196 (2011) 4109–4116.
- [3] H.K. Song, Y.H. Jung, K.H. Lee, L.H. Dao, *Electrochim. Acta* 44 (1999) 3513–3519.
- [4] H.K. Song, H.Y. Hwang, K.H. Lee, L.H. Dao, *Electrochim. Acta* 45 (2000) 2241–2257.
- [5] H.K. Song, J.H. Sung, Y.H. Jung, K.H. Lee, L.H. Dao, M.H. Kim, H.N. Kim, *J. Electrochem. Soc.* 151 (2004) E102–E109.
- [6] J.H. Jang, S. Yoon, B.H. Ka, S.M. Oh, *J. Korean Electrochem. Soc.* 6 (2003) 255–260.
- [7] J.H. Jang, S.M. Oh, *J. Electrochem. Soc.* 151 (2004) A571–A577.
- [8] J.H. Jang, S. Yoon, B.H. Ka, Y.H. Jung, S.M. Oh, *J. Electrochem. Soc.* 152 (2005) A1418–A1422.
- [9] S. Yoon, J.H. Jang, B.H. Ka, S.M. Oh, *Electrochim. Acta* 50 (2005) 2255–2262.
- [10] J.H. Jang, A. Kato, K. Machida, K. Naoi, *J. Electrochem. Soc.* 153 (2006) A321–A328.

- [11] J.H. Jang, K. Machida, Y. Kim, K. Naoi, *Electrochim. Acta* 52 (2006) 1733–1741.
- [12] J.H. Jang, S. Jeon, J.H. Cho, S.-K. Kim, S.-Y. Lee, E. Cho, H.-J. Kim, J. Han, T.-H. Lim, J. *Electrochem. Soc.* 156 (2009) B1293–B1300.
- [13] H.D. Yoo, J.H. Jang, B.H. Ka, C.K. Rhee, S.M. Oh, *Langmuir* 25 (2009) 11947–11954.
- [14] J.H. Jang, S.M. Oh, J. *Korean Electrochem. Soc.* 13 (2010) 223–234.
- [15] H.D. Yoo, Y. Park, J.H. Ryu, S.M. Oh, *Electrochim. Acta* 56 (2011) 9931–9936.
- [16] R.S. Mikhail, S. Brunauer, E.E. Bodor, J. *Colloid Interface Sci.* 26 (1968) 45–53.
- [17] H.Y. Zhu, G.Q. Lu, N. Maes, E.F. Vansant, J. *Chem. Soc. Faraday Trans.* 93 (1997) 1417–1423.
- [18] P.W. Ruch, D. Cericola, M. Hahn, R. Kotz, A. Wokaun, J. *Electroanal. Chem.* 636 (2009) 128–131.
- [19] H.D. Yoo, Ph.D. Thesis, Seoul National University, 2011.
- [20] J.A. Maciá-Agulló, B.C. Moore, D. Cazorla-Amorós, A. Linares-Solano, *Carbon* 42 (2004) 1367–1370.
- [21] N. Stribeck, *X-Ray Scattering of Soft Matter*, Springer, Berlin, 2007.
- [22] T. Kyotani, J. Chmiola, Y. Gogotsi, in: F. Beguin, E. Frackowiak (Eds.), *Carbons for Electrochemical Energy Storage and Conversion Systems*, CRC press, New York, 2010, p. 105.
- [23] J. Chmiola, G. Yushin, Y. Gogotsi, C. Portet, P. Simon, P.L. Taberna, *Science* 313 (2006) 1760–1763.
- [24] M.M. Hantel, T. Kaspar, R. Nesper, A. Wokaun, R. Köt, *Electrochem. Commun.* 13 (2011) 90–92.
- [25] X. Andrieu, in: T. Osaka, M. Datta (Eds.), *Energy Storage Systems for Electronics*, Gordon and Breach Science Publishers, 2000, p. 529.
- [26] W.G. Pell, B.E. Conway, N. Marincic, J. *Electroanal. Chem.* 491 (2000) 9–21.
- [27] H.-Q. Li, J.-Y. Luo, X.-F. Zhou, C.-Z. Yu, Y.-Y. Xia, J. *Electrochem. Soc.* 154 (2007) A731–A736.
- [28] C. Portet, P.L. Taberna, P. Simon, C. Laberty-Robert, *Electrochim. Acta* 49 (2004) 905–912.
- [29] M. Yao, K. Okuno, T. Iwaki, M. Kato, S. Tanase, K. Emura, T. Sakai, *Electrochem. Solid-State Lett.* 10 (2007) A245–A249.
- [30] Y.J. Kim, Y. Masutzuwa, S. Ozaki, M. Endo, M.S. Dresselhaus, J. *Electrochem. Soc.* 151 (2004) E199–E205.
- [31] A. Denisenko, C. Pietzka, A. Chuvilin, U. Kaiser, H. Lu, W.J. Schaff, E. Kohn, *J. Appl. Phys.* 105 (2009) 033702.
- [32] R. de Levie, *Electrochim. Acta* 8 (1963) 751–780.
- [33] H.-K. Song, J.H. Jang, J.J. Kim, S.M. Oh, *Electrochem. Commun.* 8 (2006) 1191–1196.
- [34] P.W. Ruch, R. Kotz, A. Wokaun, *Electrochim. Acta* 54 (2009) 4451–4458.
- [35] M. Hahn, O. Barbieri, R. Gallay, R. Kotz, *Carbon* 44 (2006) 2523–2533.
- [36] R. Mysyk, E. Raymundo-Pinero, F. Beguin, *Electrochem. Commun.* 11 (2009) 554–556.
- [37] D. Weingarth, A. Foelske-Schmitz, R. Köt, J. *Power Sources* 225 (2013) 84–88.
- [38] X. Yang, C. Cheng, Y. Wang, L. Qiu, D. Li, *Science* 341 (2013) 534–537.
- [39] M.D. Stoller, R.S. Ruoff, *Energy Environ. Sci.* 3 (2010) 1294–1301.
- [40] D. Aurbach, M.D. Levi, G. Salitra, N. Levy, E. Pollak, J. Muthu, J. *Electrochem. Soc.* 155 (2008) A745–A753.
- [41] J. Newman, J. *Electrochem. Soc.* 142 (1995) 97–101.
- [42] M. Eikerling, A.A. Kornyshev, E. Lust, J. *Electrochem. Soc.* 152 (2005) E24–E33.
- [43] H. Zheng, J. Li, X. Song, G. Liu, V.S. Battaglia, *Electrochim. Acta* 71 (2012) 258–265.
- [44] M.E. Suss, T.F. Baumann, M.A. Worsley, K.A. Rose, T.F. Jaramillo, M. Stadermann, J.G. Santiago, J. *Power Sources* 241 (2013) 266–273.

Glossary

A: apparent electrode area (cm^2)
 AN: acetonitrile
 A_p : peak area
 α_o : penetrability coefficient ($\text{s}^{-0.5}$)
 α_o^* : characteristic penetrability coefficient ($\text{s}^{-0.5}$)
 BF_4^- : tetrafluoroborate anion
 C : complex capacitance ($=C' + jC''$)
 C' : real part of complex capacitance ($\text{Re}[C]$)
 C'' : imaginary part of complex capacitance ($\text{Im}[C]$)
 $C_{diff,EIS}$: differential specific capacitance of an electrode by EIS analysis (F g^{-1})
 $C_{cell,EIS}$: apparent specific capacitance of a symmetric full cell by EIS analysis (F g^{-1})
 CNLS: complex nonlinear least squares
 CPE: constant phase element
 $C_{TLM}(f, \alpha_o)$: complex capacitance of a single TLM element
 $C_{TLM-PSD}$: complex capacitance of non-uniform multiple pores described by TLM-PSD
 $C_o(f, \alpha_o)$: characteristic function of a single TLM element
 C_{tot} : total capacitance of an electrode (F g^{-1})
 \bar{C}_{tot} : the average total capacitance of an electrode in the operating voltage range (F g^{-1})
 C_{util} : utilizable capacitance (F g^{-1})
 D: pore diameter (nm)
 EIS: electrochemical impedance spectroscopy
 f_{op} : operational frequency (Hz)
 f_p : peak frequency (Hz)
 ϕ : correction factor of ohmic resistance
 i : current density (mA cm^{-2})
 j : imaginary unit ($=\sqrt{-1}$)
 m : total active mass in a symmetric EDLC
 $p(\alpha_o)$: ionic accessibility profile
 PC: propylene carbonate
 pzc : potential of zero charge
 R_n : interfacial resistance of n th semicircle
 C_n : interfacial capacitance of n th semicircle
 Q_n : CPE of n th semicircle
 R_{bulk} : bulk resistance ($\Omega \text{ cm}^2$)
 R_{esr} : equivalent series resistance ($\Omega \text{ cm}^2$)
 $R_{interface}$: interfacial resistance ($\Omega \text{ cm}^2$)
 R_{ohm} : ohmic resistance ($\Omega \text{ cm}^2$)
 σ : degree of distribution
 S_{BET} : surface area measured by BET method
 TEA^+ : tetraethylammonium cation
 TLM: transmission-line model
 TLM-PSD: transmission-line model with pore size distribution
 t_{op} : operational time (s)
 V_{ohm} : ohmic voltage drop (V)
 V_{total} : total pore volume ($\text{cm}^3 \text{ g}^{-1}$)
 ω : angular frequency (rad s^{-1})
 Z : impedance
 $Z_{interface}$: interfacial impedance
 $Z_{intra-pore}$: impedance of intra-particle pores